Research Article

Xiaowen Su, Zehua Wang, Yuan Huang, Zhenyu Miao, Shuhua Wang, Jianjun Wang*, Xiao Li Zhang, Xiaomin Sun, Hong Liu, and Yuanhua Sang*

Triethanolamine interface modification of crystallized ZnO nanospheres enabling fast photocatalytic hazard-free treatment of Cr(VI) ions

https://doi.org/10.1515/ntrev-2021-0060
received May 21, 2021; accepted August 4, 2021

Abstract: The hazard-free treatment of Cr(VI) ions is critical in modern industry. Photocatalytic reduction and detoxification are high-potential strategies. Photocatalysts with high efficiency, low cost, environmental friendliness, and easy mass products are required. In this study, we report a facile strategy using triethanolamine (TEOA) as a capping ligand to modify the surface of ZnO nanospheres. The experimental and theoretical results reveal that the presence of TEOA on the surface was beneficial for electron enrichment on Zn and hole transfer to TEOA and can photocatalytically reduce Cr(VI) by almost 100% in 5 min. The photocatalytic property of TEOA-modified ZnO could be renewed by the reabsorption of TEOA in solution. The great sedimental properties benefit photocatalyst recycling and renewal, which also provides high potential for water pollution and environmental emergency responses applications.

Keywords: ZnO, surface modification, photoreduction of Cr(VI)

*** Corresponding author: Jianjun Wang,** State Key Laboratory of Crystal Materials, Shandong University, Jinan 250100, China; Shenzhen Research Institute of Shandong University, Shenzhen 518057, China, e-mail: wangjianjun@sdu.edu.cn
*** Corresponding author: Yuanhua Sang,** State Key Laboratory of Crystal Materials, Shandong University, Jinan 250100, China, e-mail: sangyh@sdu.edu.cn
Xiaowen Su, Zhenyu Miao, Shuhua Wang, Hong Liu: State Key Laboratory of Crystal Materials, Shandong University, Jinan 250100, China
Zehua Wang, Xiaomin Sun: Environment Research Institute, Shandong University, Qingdao 266237, China
Yuan Huang: State Key Laboratory of Crystal Materials, Shandong University, Jinan 250100, China; Shenzhen Research Institute of Shandong University, Shenzhen 518057, China
Xiao Li Zhang: School of Materials Science and Engineering, Zhengzhou University, Zhengzhou 450001, China

1 Introduction

Water pollution has threatened most lives on Earth. Addressing pollution by volatile organic compounds, nutrient pollutants, and heavy metals has gained the most attention. Of particular interest are heavy metals that are generally toxic and can cause major lifelong issues, especially for young people, including the hypofunction of vital organs and embryo teratism, as reported by Jomova and Valko [1]. Additionally, Islam *et al.* reported the severe situation of heavy-metal pollution in the surface water and sediment of developing countries [2]. Cr(VI) has been listed as the most toxic pollutant in water, and its removal has been a concern of researchers [3]. It comes extensively from electroplating, leather, pigments, metallurgy, and so on [4]. Due to its high solubility, it can be easily absorbed through the mouth, respiratory tract, or skin and can interfere with enzyme systems, even causing carcinogenic, teratogenic, and mutagenic effects, as discussed by Jaishankar *et al.* [5]. Fortunately, as discussed by Barrera-Diaz *et al.*, these are the toxicities of Cr(VI) instead of Cr(III), Cr(IV), and metallic Cr [6], which avoid producing secondary pollution of hazardous wastes containing high-toxicity Cr(VI). Zhang *et al.* reported a novel cellulose hydrogel coating with nanoscale Fe^0 for simultaneous Cr(VI) adsorption and reduction [7]. Therefore, the key to the treatment of wastewater containing Cr is to reduce and detoxify the content of Cr(VI). The most effective route is reducing Cr(VI) into Cr(III) through a chemical reaction and further removing Cr(III) by the precipitation process.

Generally, to remove these harmful heavy metal elements, multifarious approaches have been explored

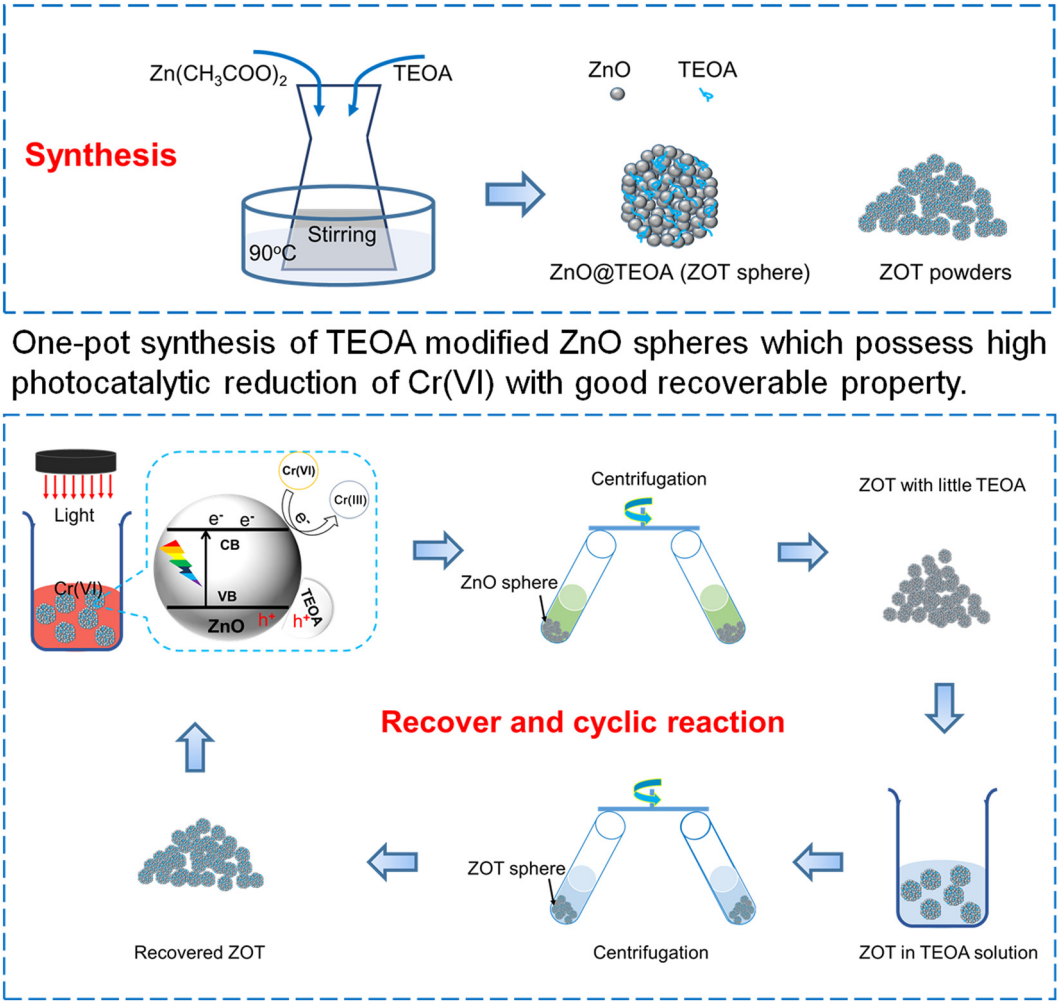

Figure 1: One-pot synthesis of TEOA-modified ZnO spheres that possess high activity for the photocatalytic reduction of Cr(VI) and good recoverable properties.

including adsorption, precipitation, membrane separation, electrodialysis, and so on. These methods abate pollution while limited by efficiency or cost. In recent years, Mezzenga *et al.* summarized sustainable technologies for water purification and heavy-metal removal [8]. As reviewed by Wang *et al.*, photocatalysis has attracted much interest in the hazard-free treatment of toxic heavy metal ions [9]. During the photocatalytic process, photoinduced electrons can participate in the reduction of high-valent metal ions into low-valent ions, even into metallic materials. For example, Zhang *et al.* realized enhanced Cr(VI) reduction with Ag-modified BiOCl nanosheets [10]. Bian *et al.* achieved the enhanced photocatalytic reduction of Cr(VI) to Cr(III) using carbon dot-coupled TiO_2 mesocrystals [11]. A UiO-66-NH_2(Zr/Hf) metal-organic framework (MOF) was also used for the photocatalytic reduction of Cr(VI) and exhibited robust properties [12]. Later, a Z-scheme UiO-66-$(COOH)_2$/$ZnIn_2S_4$ hybrid decorated with a nonnoble MoS_2 cocatalyst was proposed for photocatalytic hydrogen production and Cr(VI) reduction [13]. Metal-free semiconductors, such as graphitic carbon nitride-based photocatalysts, also possess great properties for Cr(VI) reduction [14]. The photocatalytic treatment of Cr(VI) has been considered a high-potential route to reduce Cr(VI) pollution.

ZnO is a semiconductor having a direct band gap and good photocatalytic activity, which enables water decontamination. Therefore, as a promising photocatalyst, ZnO has been widely used for dye degradation, water splitting, and photocatalytic CO_2 reduction reactions due to its high efficiency [15]. Pung *et al.* proposed the mechanisms of heavy-metal ion removal by ZnO particles, confirming the low cost and high efficiency of ZnO in Cr(VI) removal [16]. Lee *et al.* studied the photocatalytic

reduction of Cr(VI) with ZnO nanoparticles [17]. A ZnO@ZIF-8 heterostructure photocatalyst has achieved a satisfactory selective reduction of Cr(VI) [18]. Similar to the partial reaction of water splitting for H_2 production, the consumption of photoinduced electrons would enrich photoinduced holes. Then, the photoinduced electrons would be significantly suppressed. To address this issue, hole sacrificial agents, including glucose, methanol, and lactic acid, have been incorporated into the reaction system to realize reaction equilibrium [19]. However, the added pollution needs to be removed further. Mostly, the separation of photocatalysts from solution is attractive, especially for practical applications. Jiao *et al.* reported the hollow structured photocatalyst with high photocatalytic property and recycle property [20,21]. Briefly, highly efficient photoinduced charge separation and good recycling properties from solution should be important for industrial applications.

Herein, in the current work, spherical ZnO was used for the photocatalytic hazard-free treatment of Cr(VI). The photocatalytic property and the adsorption property of ZnO were used to reduce high-valent Cr and precipitate the reduced Cr products. Triethanolamine (TEOA) was used for the surface modification of ZnO to adjust the photocatalytic properties and settlement characteristics and to form the ZnO-TEOA composite (ZOT). Moreover, TEOA plays a great role in surface adsorption as a companion hole sacrificial agent, resulting in the durability of the photocatalytic reduction of Cr(VI). ZOT would be recovered with TEOA with great photocatalytic properties. The graphical abstract of the design is shown in Figure 1. We reported a one-pot synthesis of TEOA-modified ZnO spheres that possess high activity for the photocatalytic reduction of Cr(VI) and good recoverable properties. This design possesses great potential for the practical application of the photocatalytic hazard-free treatment of Cr(VI).

2 Experimental procedures

2.1 Materials

Zinc acetate ($Zn(CH_3COO)_2{\cdot}2H_2O$) was purchased from Sinopharm Chemical Reagent Co., Ltd. (Shanghai, China), triethanolamine ($C_6H_{15}NO_3$, TEOA) was purchased from Aladdin Reagent Co., Ltd. (Shanghai, China), and $K_2Cr_2O_7$ was purchased from Macklin Reagent Co., Ltd. All reagents were analytically pure and used without further purification.

2.2 Synthesis of ZnO nanospheres with TEOA

ZnO nanospheres were synthesized using a simple hydrolysis process [22]. Typically, 0.5 g of zinc acetate was added to 100 mL of purified water, and then, 5 mL of TEOA was added to the solution. After magnetic stirring for half an hour, the solution was placed in a water bath at 90°C for 2 h. The obtained ZnO was washed with deionized water and then with ethanol 3 times successively. After drying at 60°C for 12 h, the ZnO-TEOA (ZOT) sample was obtained. After being calcined at 350 and 500°C for 2 h, ZOT-350 and ZOT-500 samples were obtained.

2.3 Photocatalytic hazard-free treatment of Cr(VI)

In a typical Cr reduction experiment, the $K_2Cr_2O_7$ concentration was 30 mg/L, and a 300 W Xe simulated sunlight lamp (100 mW/cm^2) was used as the light source. Different amounts of ZnO sample were mixed with 50 mL of salt solution, and then, the solution was kept in the dark to reach absorption equilibrium in ~10 min. The concentrations of Cr(VI) in the solution were measured by UV-Vis spectrophotometry before and after photocatalysis for a certain time. The characteristic absorption peak at 375 nm of Cr(VI) was used to measure concentrations.

2.4 Characterization

The X-ray diffraction (XRD) patterns of all samples were obtained by a Bruker D8 Advance powder X-ray diffractometer (German) with Ni-filtered Cu Ka radiation, and data were collected in the 2θ range between 10° and 90° with 0.04° step intervals. Scanning electron microscopy (SEM) images were taken by a Hitachi S-4800 field-emission scanning electron microscope (Japan). The particle diameter distribution was analyzed by Nano Measurer 1.2 software (China). High-resolution transmission electron microscopy (HRTEM) was performed using a JEOL JEM 2100 microscope (Japan) operated at 200 kV. Fourier transform infrared (FTIR) spectra were recorded by a Thermo Nicolet NEXUS 670 spectrometer (USA). A spherical aberration correction transmission electron microscope (FEI Themis Z, USA) was operated at 200 kV to obtain HADDF STEM images. X-ray photoelectron spectroscopy (XPS) was performed with a Thermo ESCALAB 250XI spectrometer

(USA), and electron paramagnetic resonance (ESR) data were recorded by a JEOL JES-X320 instrument (Japan). The UV-Vis spectrophotometry used for the photocatalytic property study is UV-6100 from Shanghai Metash Instruments Co., Ltd (China).

2.5 Theoretical simulation

The experiment results performed great photocatalytic properties with the surface modification of TEOA. Therefore, we took a theoretical simulation to analyze the effect on the photocatalytic improvement of the interaction between ZnO and TEOA. In this study, we employed a (2×2) supercell with the facet of a three-atomic layer to represent bulk ZnO (101). The vacuum gap along the z-direction to the surface was 21 Å thick to prevent periodic interference of the adsorption structure and electron properties in the z-direction. The structural model had 72 atoms, including 24 Zn atoms and 24 O atoms. The DMol3 module in Materials Studio (Accelrys Inc.) was used for structure optimization and property calculations of the ZnO (101) facet [23]. The Perdew–Burke–Ernzerh (PBE) version of the general gradient approximation (GGA) was used as an exchange-correlation functional [24]. The related calculation parameters were set for the calculation of atomic charge and electrostatic potential properties. A double numerical plus polarization (DNP), as the basis set, was used to describe the valence orbital of all the atoms. A k-point mesh of $4 \times 5 \times 4$ dimensions was chosen and employed in all the calculations. The self-consistent field (SCF) density convergence was 1×10^{-6} Hartree, and a smearing setting value of 0.005 Ha was also used for acceleration.

3 Results and discussion

3.1 Morphology and structure of the spherical ZOT

The morphology and structures of the as-obtained ZOT were studied with SEM and TEM images (Figure 2). The as-synthesized ZOT particles are spherical with diameters around 350–550 nm analyzed by Nano Measurer 1.2 from the SEM image. The surface of the sphere is not smooth, which implies the assembled structure of the ZOT sphere. The TEM images (Figure 2c and the inset) show a morphology consistent with the SEM image (Figure 2a and b). The spheres are the aggregation of nanoparticles in sizes of ~20–30 nm. As is well known, the nanoparticles possess high surface energy which will drive them to assemble. The electrical double layer of ZnO is negative while the TEOA modification would reduce the electrical double layer. Therefore, the ZnO nanoparticles would prefer to assemble into large spheres with TEOA. Note that the HRTEM image (Figure 2d) shows good crystallinity inside the nanoparticles. The observed d-spacings of 2.476 and 2.814 Å can be assigned to the (101) and (100) faces of wurtzite ZnO. There is a layer of defects at the edge of the nanoparticles. The structure of the sample was further characterized using XRD, as shown in Figure 2e. All the peaks can be assigned to the diffraction

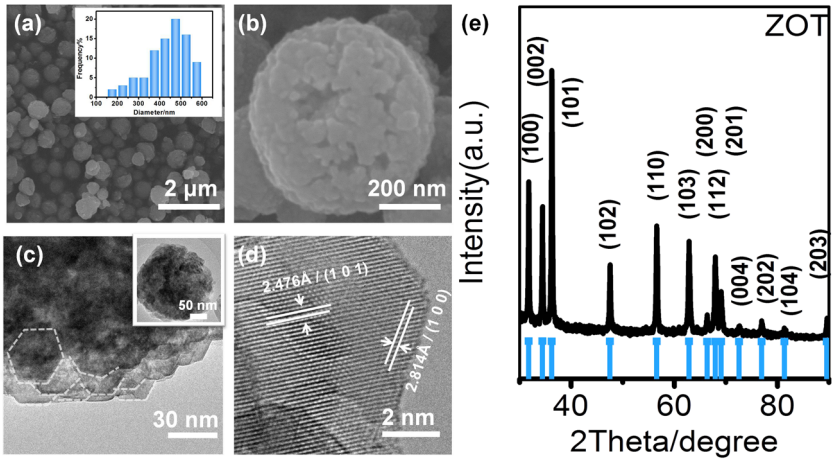

Figure 2: (a) and (b) SEM images of the as-obtained ZOT. The inset shows the sphere size distribution analyzed from the SEM image; (c) TEM image; (d) HRTEM image of the as-obtained ZOT; and (e) XRD pattern of the as-obtained ZOT.

peaks of the hexagonal wurtzite phase of ZnO (JCPDS No. 36-1451). There is no crystalline diffraction peak corresponding to other phases or compounds. The crystalline particle size is approximately 26 nm, as determined by the Scherrer formula.

3.2 Modification of TEOA in the ZnO spheres

The FTIR spectra and bonding energy of ZOT were analyzed to study the effect of TEOA (Figure 3). As shown in the FTIR spectra (Figure 3a), the band at ~3,370/cm is assigned to the surface hydroxyl groups for all the samples. The higher intensity of the ZOT sample should be due to the hydroxyl groups from TEOA [25]. Moreover, the peaks located at ~2,966 and 2,845/cm are related to the C–H symmetric and asymmetric stretching vibrations of methylene. The peak at ~1,400/cm is the C–H bonding vibration of methylene, and the peaks at ~1,071 and 1,025/cm are from C–O stretching vibrations in TEOA. Compared with that of individual TEOA, the C–H symmetric and asymmetric stretching vibrations redshift by more than 11/cm, and the C–O stretching vibrations blueshifted by more than 3/cm, which would be induced by the coordination interaction between the lone pair electrons of N atoms in TEOA and Zn atoms as well as steric hindrance [26]. No C–H stretching vibration of methylene or C═O stretching vibration is detected from ZOT-350 and ZOT-500. This indicates that the bonded TEOA was either thermally desorbed or decomposed. As shown by the XPS spectrum, a weak peak at ~399 eV corresponding to N 1s is observed (Figure 3b). TEOA is the only material with N in this system, thus indicating the presence of TEOA in the ZOT sample. Moreover, for the O 1s XPS spectrum (Figure 3c), the peak at ~529.29 eV attributed to Zn–O bonds is dominant. More peaks are analyzed at ~530.2, 531.2, and 532.0 eV, which can be ascribed to C–OH, Zn–OH, and C═O, respectively. The XPS spectrum of Zn 2p is shown in Figure 3d. A couple of peaks at 1021.9 and 1044.9 eV are present, consistent with the reported values for Zn^{2+} [27]. The presence of no other detectable peaks indicates the low defect concentration in the ZOT sample.

3.3 Photocatalytic hazard-free treatment of Cr(VI) with ZOT spheres

The photocatalytic performance of the as-synthesized samples was evaluated in 50 mL of 30 mg/L $K_2Cr_2O_7$ solution (Figure 4). Figure 4a shows that Cr(VI) can be hazard-free treated in 5 min at a catalyst concentration of 1 mg/mL.

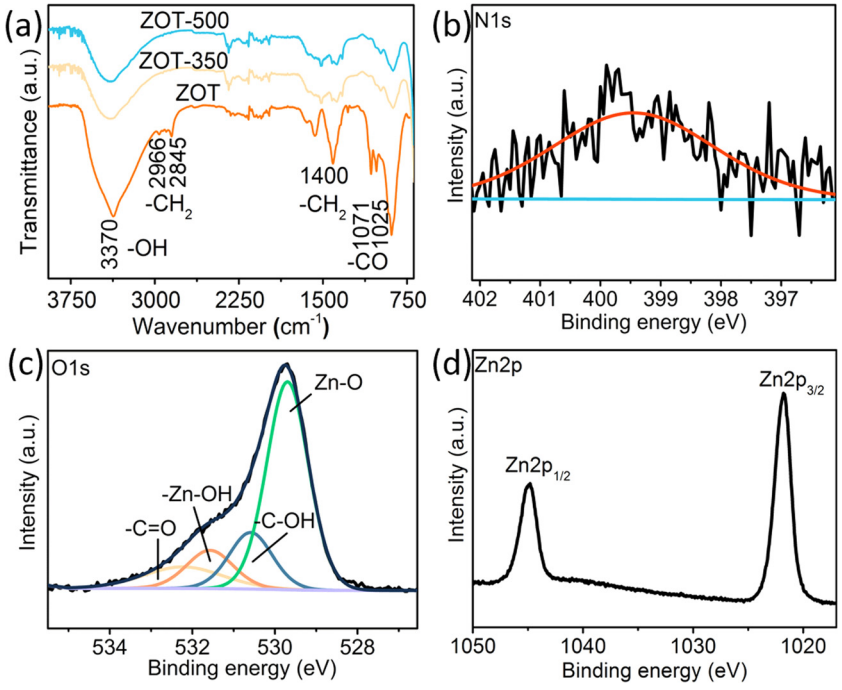

Figure 3: FTIR spectra of the samples and bonding energy of the ZOT spheres: (a) FTIR spectra of the ZOT, ZOT-350, and ZOT-500 samples; (b) XPS spectrum of N in the ZOT spheres; (c) XPS spectrum of O in the ZOT spheres; and (d) XPS spectrum of Zn in the ZOT spheres.

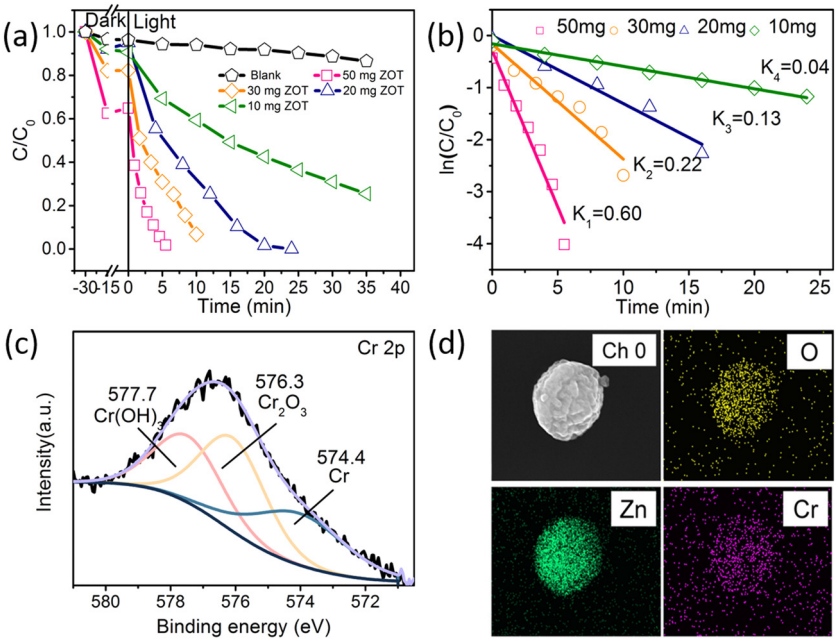

Figure 4: (a) Degradation rates of 50 mL of $K_2Cr_2O_7$ (30 mg/L) with different amounts of ZOT irradiated by a 300 W Xe lamp (100 mW/cm^2); (b) kinetic curves of $K_2Cr_2O_7$ with different amounts of ZOT analyzed from the curves shown in (a); (c) XPS spectrum of Cr on the surface of ZOT after photocatalysis; and (d) EDS mapping of ZOT after photocatalysis.

With the reduction in the catalyst amount, the time for hazard-free treatment extends. After 35 min of light irradiation, the sample with 0.2 mg/mL ZOT reduced ~70% of Cr(VI) in the solution, while only ~10% of Cr(VI) being reduced without ZOT. Before light irradiation, the absorption equivalent is achieved. Thus, this confirms the effect of ZOT on the photocatalytic reduction of Cr(VI) under light irradiation. The plots of $\ln(C/C_0)$ versus time are illustrated in Figure 4b. There were linear relationships between the two factors, with a correlation coefficient R^2 better than 0.9. This indicates that the reaction conforms to the pseudo-first-order kinetics model. The kinetic rate constant (k) values are 0.04, 0.13, 0.22, and 0.60 with 10, 20, 30, and 50 mg of ZOT catalyst, respectively. These results confirm that the reduced concentration of Cr(VI) in the solution is highly related to the ZOT photocatalyst. Moreover, after the photocatalytic treatment, the XPS spectrum of Cr on the ZOT spheres was obtained (Figure 4c). The peak at 574.4 eV indicates the existence of metallic Cr, while the peak located at 576.3 eV belongs to Cr(III) from Cr_2O_3. The peak centered at 577.7 eV could be assigned to Cr(III) from $Cr(OH)_3$[28]. No more Cr(VI) is detected on the surface of the ZOT photocatalyst, which indicates the complete reduction of Cr(VI) during the photocatalytic treatment. EDS mapping images show that Cr ions are adsorbed on the surface of ZOT nanospheres (Figure 4d). Therefore, the sample nanospheres could not only reduce heavy metals into low-valent states but also potentially remove heavy metals by their adsorption properties.

TEOA works as a hole sacrificial agent during photocatalysis. The TEOA in ZOT would be consumed and shows a decrease in the photocatalytic property. As shown in Figure 5a, the amount of Cr(VI) photocatalytically reduced with ZOT decreases from ~100 to ~20% in 5 min. The sample with TEOA in the solution shows a stable property of ~90% in 5 min. This confirms the effect of TEOA as a hole sacrificial agent, which can significantly improve the photocatalytic reduction property of ZnO. The nanoparticle-assembled ZnO spheres benefit the absorption of TEOA. Therefore, the photocatalytic property of ZOT would be renewed by the absorption of TEOA. As shown in Figure 5b, after 5 cycles, the reduction rate of Cr(VI) decreases from ~90 to ~10%. Then, the recycled ZOT was dispersed in the TEOA solution at the same concentration of the synthesis. Then, the ZOT was filtrated and used for the next photocatalytic treatment of Cr(VI). The reduction rate of Cr(VI) was renewed to ~60% and then decreased to ~45 and ~30% for the next 2 cycles. Moreover, after 5 cycles, the Cr(VI) reduction rate of the renewed ZOT with TEOA is ~10% again (Figure 5c). Fortunately, after renewal with TEOA again, the photocatalytic property recovers to ~60%, which is the same as that of the first renewal process. It possesses the same

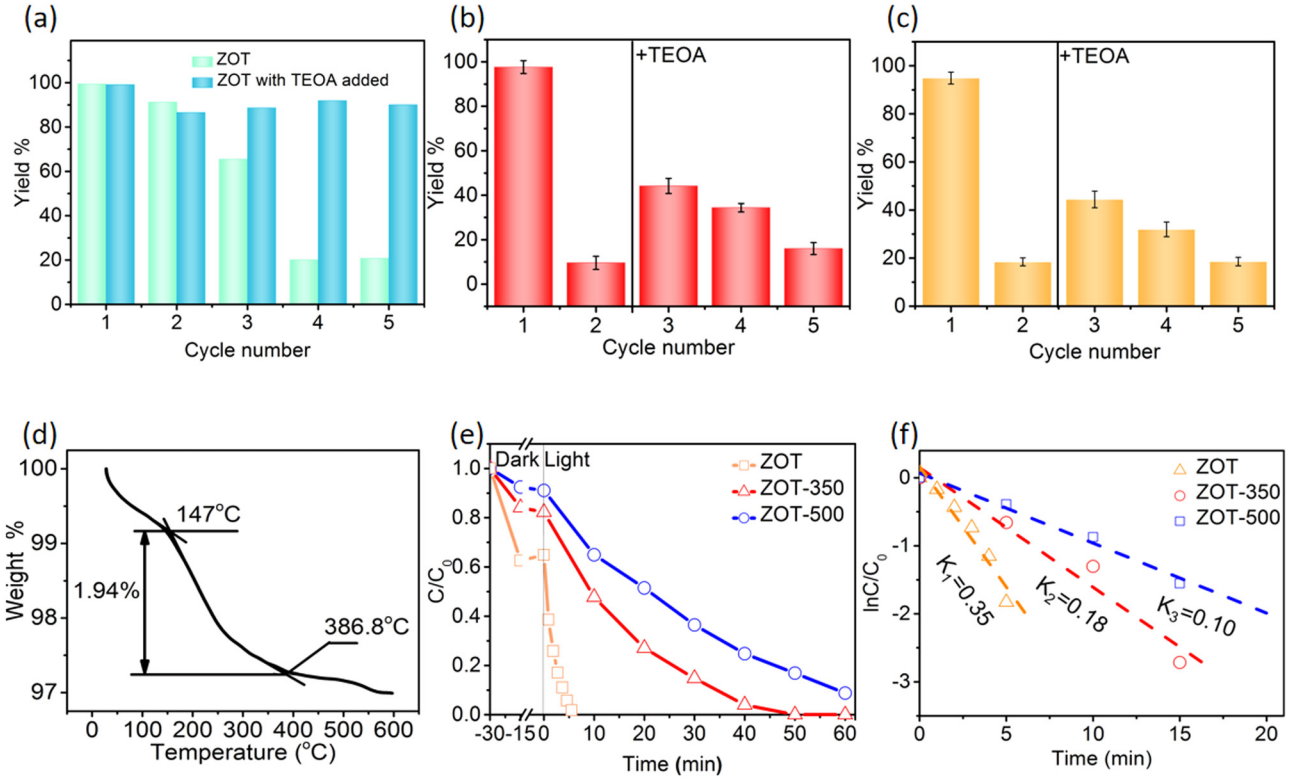

Figure 5: (a) Cyclic photocatalytic reductions of Cr(VI) with ZOT and TEOA or ZOT alone in the solution in 5 min and the cyclic performance; (b) renewal of ZOT by the adsorption of TEOA after 5 cycles; (c) renewal of ZOT by the adsorption of TEOA after 10 cycles; (d) TG curve of as-synthesized ZOT; (e) photocatalytic reduction rates of $K_2Cr_2O_7$ (30 mg/L) with 50 mg of ZOT, ZOT-350, and ZOT-500 in a 50 mL solution; and (f) kinetic curves of ZOT, ZOT-350, and ZOT-500 analyzed from the curves shown in (e).

property in that the photocatalytic property decreases from ~60 to ~45% and ~30%. The results indicate that the property can simply be renewed by the absorption of TEOA. Moreover, the authors compared this photocatalytic property with other works as shown in Table 1. The ZOT performs the best property. Figure 5d shows the TG curve of ZOT. There is ~1.94% weight loss between 147 and 386°C, which is assigned to the absorbed TEOA in ZOT. ZOT was calcined at 350 and 500°C to remove the TEOA in ZOT, according to the TG curve. Figure 5e shows the photocatalytic reduction of Cr(VI) with ZOT, ZOT-350, and ZOT-500. ZOT possesses the best property, while ZOT-500 possesses the worst property. The photocatalytic reduction kinetics were analyzed by the plots of $\ln(C/C_0)$ versus time in Figure 5f. The kinetic rate constant k is 0.354/min for ZOT, which is twice or three times the corresponding values of ZOT-350 and ZOT-500, 0.176 and 0.103/min, respectively. These results indicated that the

Table 1: Comparative performance for photocatalysts for Cr reduction

Photocatalysts	Experimental condition				Efficiency (%)	Ref.
	Dose (mg)	Volume (mL)	Concentration (mg/L)	Time (min)		
BUC-21/$Bi_{24}O_{31}Br_{10}$	50	200	10	120	99	[29]
CoS_2/g-C_3N_4-rGO	10	20	20	150	98	[30]
BPTCN	50	50	10	60	95	[31]
CdS/$CuInS_2$	30	150	10	60	~100	[32]
g-C_3N_4/UiO-66	100	200	10	40	99	[33]
CoFe-LDH/g-C_3N_4	50	50	50	100	100	[34]
ZOT	50	50	30	5	~100	This work

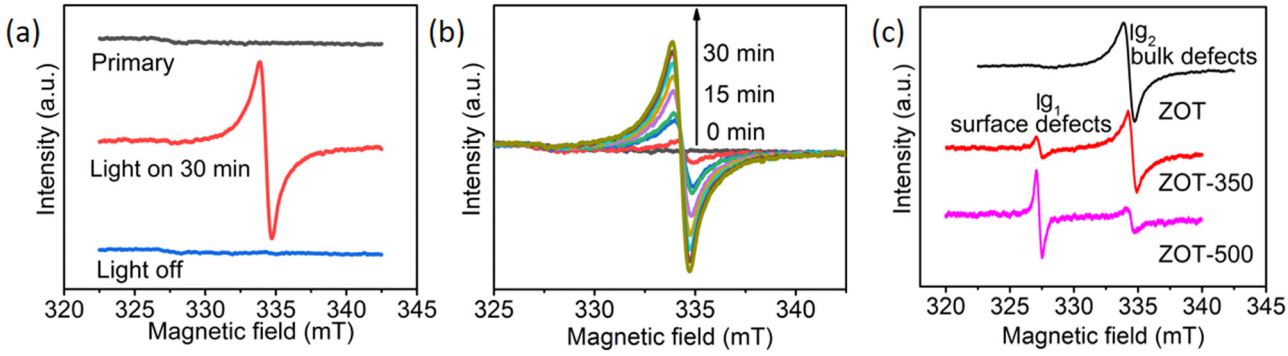

Figure 6: ESR spectra of (a) ZOT before, during, and after light irradiation for 30 min; (b) ZOT under light irradiation for various times; and (c) ZOT, ZOT-350, and ZOT-500 under light irradiation for 20 min.

TEOA molecules on the surface of ZnO play a key role in the separation of photogenerated carriers, subsequently improving the photocatalytic efficiency.

3.4 Mechanism of the various photocatalytic properties of ZOT spheres

The photocatalytic mechanism was investigated based on the ESR spectra (Figure 6). As shown in Figure 6a, there was no detected ESR peak for the ZOT sample in the dark. With light irradiation, there is an obvious peak with a g value of 1.9560 (g_1). This should be attributed to the oxygen vacancy (Vo+) [35] because it is a light-sensitive center and can only be observed under light irradiation. A similar phenomenon has been detected in other photocatalytic processes [36,37]. Notably, the ESR peak intensity increased with continuous light irradiation (Figure 6b). The reason for this Vo+ increase under light irradiation would be due to the existence of TEOA. Because TEOA is a reductant, it would benefit the formation of Vo+ during the photocatalytic process. More photoinduced electrons would be released and benefit the photocatalytic reduction process. After removing TEOA by calcination, the ESR spectra are recorded (Figure 6c). A new peak with a g value of 1.9981 (g_2) is detected in both the ZOT-350 and ZOT-500 samples and can be assigned to the unpaired electron trapped in a surface oxygen ion vacancy or the Zn^+ ion [38]. Notably, the g_1/g_2 intensity ratios of the two samples are different. With increasing calcination temperature, g_1 becomes more significant. According to the TG curve of ZOT, TEOA quickly oxidizes at temperatures over 380°C. The reduction of ZnO at 350°C is weaker than that at 500°C. Therefore, the surface defect concentration of the particles is lower at 350°C than at 500°C. This also implies that the TEOA in the as-synthesized ZOT is at the interfaces between particles. Interestingly, no surface defect g_1 ESR signal was observed from ZOT, even under light irradiation, which was probably due to the capping effect of TEOA.

As shown in the XRD pattern (Figure 1e), the main crystal plane is the (101) plane. Therefore, the electrostatic potentials between TEOA and the (101) plane of ZnO were analyzed by the DMol3 module (Figure 7). The Zn atom possesses a +0.934 eV Mulliken charge under the initial conditions of the ZnO surface, as shown in Figure 7a. During light irradiation, there were oxygen vacancies in ZnO. The existence of a single oxygen

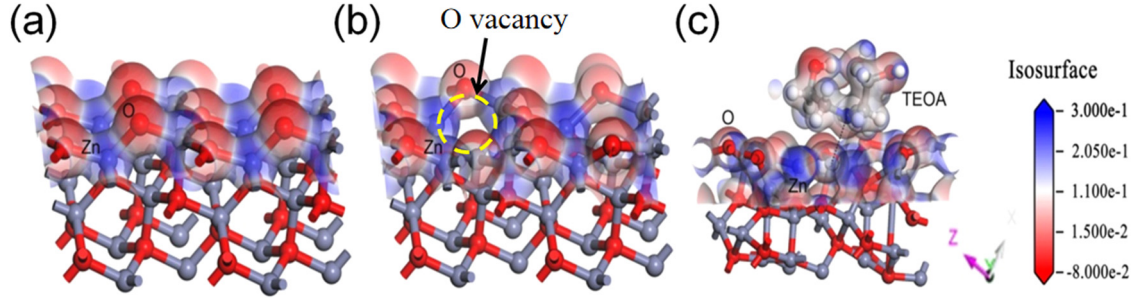

Figure 7: Schematic diagram of the (a) (101) plane of the initial ZnO, (b) (101) plane of ZnO with a single oxygen vacancy, and (c) (101) plane of ZnO with a single oxygen vacancy coupled with a TEOA molecule.

vacancy can influence the Mulliken charge on the Zn atom, decreasing it to +0.851 eV (Figure 7b). This confirms the effect of light irradiation on the electron structure of ZnO. When a N atom from TEOA is adsorbed at the oxygen vacancy, the Mulliken charge of Zn further decreases to +0.773, as shown in Figure 7c. The coordination interaction between an unshared electron pair of a N atom in TEOA and surface Zn atoms can affect the electron density distribution around the bonded Zn atom and the charge state on each atom. The change in Mulliken charge confirms the interaction between TEOA and ZnO under light irradiation. This result can support the discussion of the photocatalytic process with TEOA. Obviously, the transfer of holes to TEOA also makes the hole sacrificial agent more efficient, improving the photocatalytic reduction of Cr(VI) with ZOT.

4 Conclusion

ZnO nanospheres modified by TEOA were synthesized *via* a simple hydrolysis process. The as-prepared ZnO sample was modified by TEOA. It possessed a high photocatalytic reduction efficiency for the hazard-free treatment of Cr(VI) ions in water. The full reduction of Cr(VI) required only ~5 min. The photocatalytic property of TEOA-modified ZnO could be renewed by the reabsorption of TEOA in solution. Surface modification with TEOA promoted the electron density enhancement of atoms adjacent to the TEOA molecule, which makes the hole sacrificial agent effect of TEOA work efficiently. The great sedimental properties benefit photocatalyst recycling and renewal, which also provides great potential for practical applications. A system that can realize the quasi-continuable photocatalytic hazard-free treatment of Cr(VI) ions with ZOT should be designed based on the advantages and properties of ZOT spheres.

Funding information: This work was supported by the National Natural Science Foundation of China (Grant Nos. 52072223, 21802086, and 51732007), the Shandong Provincial Natural Science Foundation (Grant No. ZR2019MB048), and the Beijing National Laboratory for Molecular Sciences Program (BNLMS201802). Financial support from the Shenzhen Basic Research Program (No. JCYJ20190807-093411445) is acknowledged.

Author contributions: All authors have accepted responsibility for the entire content of this manuscript and approved its submission.

Conflict of interest: The authors state no conflict of interest.

References

[1] Jomova K, Valko M. Advances in metal-induced oxidative stress and human disease. Toxicology. 2011;283(2–3):65–87.
[2] Islam MS, Ahmed MK, Raknuzzaman M, Habibullah-Al-Mamun M, Islam MK. Heavy metal pollution in surface water and sediment: a preliminary assessment of an urban river in a developing country. Ecol Indic. 2015;48:282–91.
[3] Fernandez PM, Vinarta SC, Bernal AR, Cruz EL, Figueroa LIC. Bioremediation strategies for chromium removal: current research, scale-up approach and future perspectives. Chemosphere. 2018;208:139–48.
[4] Chai L, Huang S, Yang Z, Peng B, Huang Y, Chen Y. Cr(VI) remediation by indigenous bacteria in soils contaminated by chromium-containing slag. J Hazard Mater. 2009;167(1–3):516–22.
[5] Jaishankar M, Tseten T, Anbalagan N, Mathew BB, Beeregowda KN. Toxicity, mechanism and health effects of some heavy metals. Interdiscip Toxicol. 2014;7(2):60–72.
[6] Barrera-Diaz CE, Lugo-Lugo V, Bilyeu B. A review of chemical, electrochemical and biological methods for aqueous Cr(VI) reduction. J Hazard Mater. 2012;223:1–12.
[7] Wang Y, Yu L, Wang R, Wang Y, Zhang X. A novel cellulose hydrogel coating with nanoscale Fe^0 for Cr(VI) adsorption and reduction. Sci Total Environ. 2020;726:138625.
[8] Bolisetty S, Peydayesh M, Mezzenga R. Sustainable technologies for water purification from heavy metals: review and analysis. Chem Soc Rev. 2019;48(2):463–87.
[9] Wang C-C, Du X-D, Li J, Guo X-X, Wang P, Zhang J. Photocatalytic Cr(VI) reduction in metal-organic frameworks: a mini-review. Appl Catal B Environ. 2016;193:198–216.
[10] Li H, Zhang L. Oxygen vacancy induced selective silver deposition on the {001} facets of BiOCl single-crystalline nanosheets for enhanced Cr(VI) and sodium pentachlorophenate removal under visible light. Nanoscale. 2014;6(14):7805–10.
[11] Zhang Y, Xu M, Li H, Ge H, Bian Z. The enhanced photoreduction of Cr(VI) to Cr(III) using carbon dots coupled TiO_2 mesocrystals. Appl Catal B Environ. 2018;226:213–9.
[12] Du X-D, Yi X-H, Wang P, Zheng W, Deng J, Wang C-C. Robust photocatalytic reduction of Cr(VI) on UiO-66-NH_2(Zr/Hf) metal-organic framework membrane under sunlight irradiation. Chem Eng J. 2019;356:393–9.
[13] Mu F, Cai Q, Hu H, Wang J, Wang Y, Zhou S, et al. Construction of 3D hierarchical microarchitectures of Z-scheme UiO-66-$(COOH)_2$/$ZnIn_2S_4$ hybrid decorated with non-noble MoS_2 cocatalyst: a highly efficient photocatalyst for hydrogen evolution and Cr(VI) reduction. Chem Eng J. 2020;384:123352.
[14] Wang Z, Murugananthan M, Zhang Y. Graphitic carbon nitride based photocatalysis for redox conversion of arsenic(III) and chromium(VI) in acid aqueous solution. Appl Catal B Environ. 2019;248:349–56.
[15] Kamat PV, Huehn R, Nicolaescu R. A "sense and shoot" approach for photocatalytic degradation of organic contaminants in water. J Phys Chem B. 2002;106(4):788–94.

[16] Le AT, Pung SY, Sreekantan S, Matsuda A, Huynh DP. Mechanisms of removal of heavy metal ions by ZnO particles. Heliyon. 2019;5(4):e01440.
[17] Siboni MS, Samadi MT, Yang JK, Lee SM. Photocatalytic reduction of Cr(VI) and Ni(II) in aqueous solution by synthesized nanoparticle ZnO under ultraviolet light irradiation: a kinetic study. Environ Technol. 2011;32(13–14):1573–79.
[18] Wang X, Liu J, Leong S, Lin X, Wei J, Kong B, et al. Rapid construction of ZnO@ZIF-8 heterostructures with size-selective photocatalysis properties. ACS Appl Mater Interfaces. 2016;8(14):9080–87.
[19] Kretschmer I, Senn AM, Meichtry JM, Custo G, Halac EB, Dillert R, et al. Photocatalytic reduction of Cr(VI) on hematite nanoparticles in the presence of oxalate and citrate. Appl Catal B Environ. 2019;242:218–26.
[20] Jiao W, Wang LZ, Liu G, Lu GQ, Cheng HM. Hollow anatase TiO_2 single crystals and mesocrystals with dominant {101} facets for improved photocatalysis activity and tuned reaction preference. ACS Catalysis. 2012;2:1854–9.
[21] Jiao W, Xie YP, Chen RZ, Zhen C, Liu G, Ma XL, et al. Synthesis of mesoporous single crystal rutile TiO_2 with improved photocatalytic and photoelectrochemical activities. ChemComm. 2013;49:11770–2.
[22] Zak AK, Razali R, Majid WHA, Darroudi M. Synthesis and characterization of a narrow size distribution of zinc oxide nanoparticles. Int J Nanomed. 2011;6:1399–403.
[23] Delley B. From molecules to solids with the DMol(3) approach. J Chem Phys. 2000;113(18):7756–64.
[24] Perdew JP, Chevary JA, Vosko SH, Jackson KA, Pederson MR, Singh DJ, et al. Atoms, molecules, solids, and surfaces: applications of the generalized gradient approximation for exchange and correlation. Phys Rev B. 1992;46(11):6671–87.
[25] Haque MA, Mahalakshmi S. Effect of triethanolamine on zinc oxide nanoparticles. Mater Focus. 2013;2(6):469–74.
[26] Kim H, Gim S, Jeon TH, Kim H, Choi W. Distorted carbon nitride structure with substituted benzene moieties for enhanced visible light photocatalytic activities. ACS Appl Mater Interfaces. 2017;9(46):40360–8.
[27] Le S, Jiang T, Li Y, Zhao Q, Li Y, Fang W, et al. Highly efficient visible-light-driven mesoporous graphitic carbon nitride/ZnO nanocomposite photocatalysts. Appl Catal B Environ. 2017;200:601–10.
[28] Askarian M, Peikari M, Javadpour S. Dichromate effect on the passive layer of 316L stainless steel. Surf Eff Contact Mech IX. 2009;62:27–36.
[29] Zhao C, Wang Z, Li X, Yi X, Chu H, Chen X, et al. Facile fabrication of BUC-21/$Bi_{24}O_{31}Br_{10}$ composites for enhanced photocatalytic Cr(VI) reduction under white light. Chem Eng J. 2020;389:123431.
[30] Wang Y, Bao S, Liu Y, Yang W, Yu Y, Feng M, et al. Efficient photocatalytic reduction of Cr(VI) in aqueous solution over CoS_2/g-C_3N_4-rGO nanocomposites under visible light. Appl Surf Sci. 2020;510:145495.
[31] Wang W, Niu Q, Zeng G, Zhang C, Huang D, Shao B, et al. 1D porous tubular g-C_3N_4 capture black phosphorus quantum dots as 1D/0D metal-free photocatalysts for oxytetracycline hydrochloride degradation and hexavalent chromium reduction. Appl Catal B Environ. 2020;273:119051.
[32] Deng F, Lu X, Luo Y, Wang J, Che W, Yang R, et al. Novel visible-light-driven direct Z-scheme CdS/$CuInS_2$ nanoplates for excellent photocatalytic degradation performance and highly-efficient Cr(VI) reduction. Chem Eng J. 2019;361:1451–61.
[33] Yi XH, Ma SQ, Du XD, Zhao C, Fu H, Wang P, et al. The facile fabrication of 2D/3D Z-scheme g-C_3N_4/UiO-66 heterojunction with enhanced photocatalytic Cr(VI) reduction performance under white light. Chem Eng J. 2019;375:121944.
[34] Ou B, Wang J, Wu Y, Zhao S, Wang Z. Efficient removal of Cr(VI) by magnetic and recyclable calcined CoFe-LDH/g-C_3N_4 via the synergy of adsorption and photocatalysis under visible light. Chem Eng J. 2020;380:122600.
[35] Liu D, Lv YH, Zhang M, Liu YF, Zhu YY, Zong RL, et al. Defect-related photoluminescence and photocatalytic properties of porous ZnO nanosheets. J Mater Chem A. 2014;2(37):15377–88.
[36] Neykova N, Chang Y-Y, Buryi M, Davydova M, Kucerkova R, Simek D, et al. Study of ZnO nanorods grown under UV irradiation. Appl Surf Sci. 2019;472:105–11.
[37] Jakes P, Erdem E. Finite size effects in ZnO nanoparticles: an electron paramagnetic resonance (EPR) analysis. Phys Status Solidi Rapid Res Lett. 2011;5(2):56–8.
[38] Ischenko V, Polarz S, Grote D, Stavarache V, Fink K, Driess M. Zinc oxide nanoparticles with defects. Adv Funct Mater. 2005;15(12):1945–54.